ENGINEERING Environment
2026, 20(4): 54 https://doi.org/10.1007/s11783-026-2154-4

RESEARCH ARTICLE

Unraveling mechanisms of mechanical shear stress-regulated high nitrite production in denitrification: granular structure and metagenomic evidence

Jiarui Fan[1], Shenbin Cao[2], Xiangchen Li[3], Yongzhen Peng[1], Rui Du ✉ [1]

1. National Engineering Laboratory for Advanced Municipal Wastewater Treatment and Reuse Technology, Engineering Research Center of Beijing, Beijing University of Technology, Beijing 100124, China
2. College of Architecture and Civil engineering, Beijing University of Technology, Beijing 100124, China
3. Sinopec Beijing Research Institute of Chemical Industry, Beijing 100013, China

HIGHLIGHTS

- High nitrite production rate of 7.7 kg N/(m^3·d) was achieved in denitrification system.
- Low shear stress improved NO_2^- by rising electron transfer and bacterial activity.
- Slowly reducing influent NO_3^- under low shear stress restored NO_2^- accumulation.
- Micro-CT revealed mineralized cores with surface pits promoted PD granulation.
- High shear stress and NLR facilitated the enrichment of dominant bacteria *Thauera*.

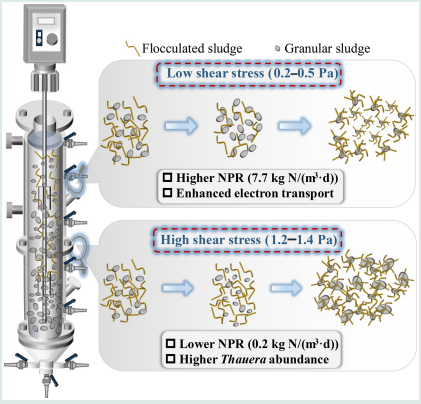

ABSTRACT: Partial denitrification granules (PDG) offer a novel approach to supplying nitrite (NO_2^-) for anammox. Shear stress (τ) induced by mechanical stirring has been recognized as an effective operational strategy for enhancing mass transfer in continuous-flow PDG systems with minimal gas production. However, the effects of shear stress intensity on nitrite (NO_2^-) accumulation, granular structure, and microbial succession remains unclear. This study established two continuously up-flow PDG systems to assess the influence of low-strength τ (0.2–0.5 Pa) and high-strength τ (1.2–1.4 Pa) on PDG performance under dynamic nitrate (NO_3^-) loading rates (NLR). Results indicated that low-strength τ promoted the formation of 1–2 mm granules, mitigating the washout of flocs and smaller granules, and sustaining a stable nitrite production rate (NPR) of 7.7 kg N/(m^3·d) at an NLR as high as 11.7 kg N/(m^3·d). In contrast, high-strength τ caused particle fragmentation and reaggregation, accompanied by the washout of sludge containing PD bacteria, leading to a lower NPR of 0.2 kg N/(m^3·d). Metagenomic analysis revealed that low-strength τ enhanced nitrogen-carbon metabolism, with *Thauera*.sp. and *Thauera*_phenylacetica synergistically driving NO_2^- accumulation. Although high-strength τ promoted the enrichment of *Thauera* (~70%), *Thauera*.sp. decreased its contribution to *napA* and improved to *nirK*, whereas *Thauera*_phenylacetica reduced its contribution to *napA*, thereby constraining NO_2^- accumulation. These findings provide critical insights into optimizing shear conditions for PDG and enhance the understanding of the metagenomic mechanisms of PD.

✉ Corresponding author. E-mail: durui@bjut.edu.cn
Article history: Received 27 May 2025, Revised 24 September 2025, Accepted 23 November 2025, Available online 20 January 2026

KEYWORDS: Shear stress (τ), Partial denitrification, Nitrite production rate, Granular structure, Metabolic mechanism

1 Introduction

The discharge of wastewater is steadily increasing, and the biological treatment of nitrogen-containing wastewater remains a significant challenge (Liu et al., 2024; Qu and Chen, 2024). Integrated partial denitrification with anaerobic ammonia oxidation (PD/A) technology has emerged as an energy-efficient and environmentally friendly approach for removing ammonia (NH_4^+) and nitrate (NO_3^-), requiring less energy and carbon source demand compared to traditional nitrogen removal methods (Du et al., 2017). The underlying principle of PD/A technology involves reducing NO_3^- to nitrite (NO_2^-) during the partial denitrification (PD) process, follow by the conversion of NO_2^- to nitrogen (N_2) by anammox bacteria using NH_4^+ as an electron donor. This process effectively decreases aeration needs, sludge generation, organic carbon feeding, and mitigates nitrous oxide (N_2O) emissions (Al-Hazmi et al., 2023; Sun et al., 2025). Consequently, this innovative technology holds significant potential for advancing the sustainable development of wastewater treatment (Huang et al., 2024).

Nevertheless, the dynamic characteristics of nitrate loading rates (NLR) in real wastewater pose significant challenges to the stability of NO_2^- accumulation in PD systems, which in turn affected the substrate supply for anammox (Cao et al., 2021). Continuous-flow reactors, renowned for their superior resistance to shock loading and operational convenience, have become the predominant configuration for achieving high-rate nitrogen removal (Bode et al., 1987; Feng et al., 2025). Previous studies have demonstrated that a nitrogen removal rate (NRR) of 11.25 kg $NO_3^-/(m^3 \cdot d)$ was achieved in an anoxic up-flow sludge bed (Franco et al., 2006), while an anammox USB attained an exceptional NRR of 74.3–76.7 kg $NO_3^-/(m^3 \cdot d)$ (Tang et al., 2011). These findings underscored the adaptability of continuous-flow systems in addressing fluctuating nitrogen loads, as well as the excellent potential for advanced nitrogen removal. However, the lack of gas generation in the PD process can spontaneously result in insufficient mass transfer and sludge flotation, thereby undermining the stability of PD granules (PDG) and posing significant constraints on the engineering application of continuous-flow systems.

Recent research has shown that horizontal shear stress generated by mechanical mixing can effectively enhance mass transfer and successfully cultivate PDG, achieving a high nitrite production rate (NPR) of 2.66 kg $N/(m^3 \cdot d)$, thereby laying a solid foundation for the efficient operation of the PD/A process (Fan et al., 2024a). Notably, shear stress (τ) generated by mechanical mixing serves as a critical operational parameter in granular sludge systems, and its dynamic regulatory mechanism significantly influences biomass concentration and the stability of granular sludge. Previous studies have shown that lower τ in continuous-flow reactors can preserve sludge granulation (Hou et al., 2014; Wang et al., 2022). Conversely, higher-strength τ can fragment granules into smaller particles, increasing their permeability and enhancing mass transfer (Zhang et al., 2013; Wang et al., 2022). However, the impact of mechanical mixing intensity regulated by τ on NO_2^- accumulation and the succession of microbial consortia in PDG within a continuous-flow system remains unclear, particularly under dynamic NLR conditions. Identifying an optimal range of mechanical mixing intensity is crucial for cultivating stable and high-rate PDG in continuous-flow reactors.

Therefore, this study systematically investigated the impact of varying mechanical mixing intensities on the multiscale influencing mechanisms of PDG under gradient NLR. For the first time, the internal nucleus structure of PDG was visualized using microbial computed tomography (micro-CT). The chemical composition of the inorganic core structure was characterized through X-ray Diffraction (XRD), X-ray Photoelectron Spectroscopy (XPS), and Raman spectroscopy. Furthermore, the evolution of microbial communities and the response mechanisms of functional bacteria and nitrogen-carbon metabolic functional genes were further analyzed under shear stress-driven conditions. This study offered comprehensive insights into the shear stress-regulated granular structure and microbial succession of PD under dynamic NLR, providing valuable guidance for operational optimization in continuous-flow PD/A systems.

2 Materials and methods

2.1 Reactor operation

The experiment was conducted in two identical up-flow continuous stirring reactors, designated as UCS-1 and

UCS-2, each with an effective volume of 4 L. UCS-1 was operated under low-strength τ (0.2–0.5 Pa), while UCS-2 was operated under high-strength τ (1.2–1.4 Pa). A mechanical agitator equipped with four rectangular blades was installed in each reactor. τ generated could be precisely controlled by adjusting the speed of the mechanical agitator to prevent sludge flotation (Fig. S1). The method used to calculate τ was based on previous reports (Pinho et al., 1997; Wang et al., 2022), and the detailed information was shown in Text S1. Additionally, temperature and pH were not controlled during operation. The hydraulic retention time (HRT) in UCS-1 was consistently maintained at 2 h, while the HRT in UCS-2 was set at 3 h during days 106–113 and 2 h for all other periods.

2.2 Sludge and synthetic wastewater

The seeding sludge was obtained from a denitrifying sequencing batch reactor (SBR) operating under an NLR of 2.21 kg N/(m^3·d), with a nitrate-to-nitrite transformation ratio (NTR) of up to 83% (Fan et al., 2024b). The sludge granules exhibited relatively regular shapes, with an average diameter of 1124 μm. The mixed liquor suspended solids (MLSS) of inoculated sludge in UCS-1 and UCS-2 were 36.3 and 41.1 g, respectively.

Synthetic wastewater with the influent NO_3^--N concentrations ranging from 30 to 1000 mg/L was fed to both reactors. The detailed composition was provided in Table S1. Sodium acetate served as the electron donor for the reduction of NO_3^-. The entire experiment was operated for 232 days and divided into four phases. The detailed operating parameters were listed in Table 1 and Table 2.

2.3 Activity of denitrifying bacteria

At various influent NO_3^--N concentrations throughout the operation, granular and flocculent sludge were collected from the two reactors and transferred to 500 mL glass containers to evaluate the activity of denitrifying bacteria. The influent NO_3^--N concentration was set at 30 mg/L with a COD/NO_3^--N ratio of

Table 1 Operating condition in UCS-1

Phase (d)	τ (Pa)	Inf. NO_3^--N (mg/L)	NLR (kg N/(m^3·d))	NPR (kg N/(m^3·d))	NTR (%)
I (1–28)	0.7	32±1.8	0.4	0.1	24.5
II-i (29–61)	0.2	63.2±1.8	0.8	0.3	44
II-ii (62–90)		97.6±6.8	1.2±0.1	0.5±0.1	46.4
II-iii (91–117)	0.2–0.5	296.9±8.4	3.6±0.1	1.9±0.2	55.5
III-i (118–134)	0.5–1.1	581.5±25.3	7±0.3	4.4±0.2	63.8
III-ii (135–141)	1.1	297.2±6	3.6±0.1	0.03	2
III-iii (142–157)	0.2	98.4±1.4	1.2	0.5±0.1	48
IV-i (158–170)	0.5	300.3±8.5	3.6±0.1	2.1±0.1	61.5
IV-ii (171–211)		587.9±19.5	7.1±0.2	3.9±0.6	65.2
IV-iii (212–232)		974.9±43.9	11.7±0.5	7.7±1	72.5

Table 2 Operating condition in UCS-2

Phase (d)	τ (Pa)	Inf. NO_3^--N (mg/L)	NLR (kg N/(m^3·d))	NPR (kg N/(m^3·d))	NTR (%)
I (1–28)	0.7	32±1.8	0.4	0.1	22.5
II-i (29–61)	1.2	63.2±1.8	0.8	0.3±0.1	37.1
II-ii (62–90)		97.6±6.8	1.2±0.1	0.5±0.1	46.6
II-iii (91–117)	1.2–1.4	296.6±8.6	3.2±0.6	1.6±0.3	48.5
III-i (118–134)	0.2–1.6	581.5±25.3	7±0.3	0.2±0.4	3.6
III-ii (135–141)	0.2	297.2±6	3.6±0.1	0.6±0.6	28.2
III-iii (142–157)		98.4±1.4	1.2	0.4±0.1	35.5
IV-i (158–170)	1.4	300.3±8.5	3.6±0.1	2.2±0.1	64.1
IV-ii (171–211)		586.9±19.5	7.1±0.2	3.7±0.5	62.2
IV-iii (212–232)		968.9±43.4	11.6±0.5	0.2±0.2	16.8

3. Samples were taken and filtered at regular intervals for testing. The activity was evaluated by measuring the maximum denitrification rates, including the specific nitrate reduction rate (r_{NO_3}) and the specific nitrite accumulation rate (r_{NO_2}). The r_{NO_3} and r_{NO_2} of granular and flocculated sludge under different τ and NLR conditions were fitted and analyzed using TableCurve 3D software.

2.4 Calculation

2.4.1 Nitrogen conversion activity

$$r_{NO_3} = [c(NO_3^-\text{-}N_1) - c(NO_3^-N_2)]/(t_2 - t_1)/\text{MLVSS}, \quad (1)$$

$$r_{NO_2} = [c(NO_2^-\text{-}N_2) - c(NO_2^-\text{-}N_1)]/(t_2 - t_1)/\text{MLVSS}, \quad (2)$$

where $c(NO_3^-\text{-}N_1)$ and $c(NO_3^-\text{-}N_2)$ represent the initial NO_3^--N concentration and NO_3^--N concentration corresponding to the maximum accumulation of NO_2^--N, respectively. $c(NO_2^-\text{-}N_1)$ and $c(NO_2^-\text{-}N_2)$ represent the initial NO_2^--N concentration and the maximum NO_2^--N accumulation concentration, respectively.

2.4.2 Nitrogen loading rate and nitrite production efficiency

$$\text{NLR} = c(NO_3^-\text{-}N)_{inf} \times \text{HRT} \times 24/V, \quad (3)$$

$$\text{NPR} = c(NO_2^-\text{-}N)_{eff} \times \text{HRT} \times 24/V, \quad (4)$$

$$\text{NTR} = c(NO_2^-\text{-}N)_{eff}/(c(NO_3^-\text{-}N)_{inf} - c(NO_3^-\text{-}N)_{eff}), \quad (5)$$

where $c(NO_3^-\text{-}N)_{inf}$, $c(NO_3^-\text{-}N)_{eff}$, and $c(NO_2^-\text{-}N)_{eff}$ represent the influent NO_3^--N concentration, effluent NO_3^--N concentration, and effluent NO_2^--N concentration, respectively, and V represents the effective volume of the reactor.

2.5 Surface morphology and inorganic core structure of PDG

The surface morphology and inorganic core structure were examined using a scanning electron microscope (SEM), and the element composition was quantitatively analyzed with an energy dispersive spectrometer. The spatial distribution profile of PDG was analyzed using the micro-CT techniques, and the three-dimensional image of its internal core structure was reconstructed from two-dimensional cross-section slices. The sample preparation involved immersion in a 2.5% glutaraldehyde solution for 1.5 h, followed by dehydration in a graded series of 50%, 70%, and 100% ethanol. The samples were then dried and scanned at a voltage of 30 kV, a current of 50 μA, and a resolution of 2 μm (Guo et al., 2021).

2.6 Physico-chemical characterization of PDG

Samples were collected regularly, filtered through 0.45 μm qualitative filter paper, and promptly stored in a 4 °C refrigerator. Concentrations of NO_3^--N, NO_2^--N, MLSS, and MLVSS were determined using standard methods, while chemical oxygen demand (COD) was analyzed using a COD quick-analysis instrument. The extracellular polymeric substances (EPS), which included soluble EPS (S-EPS), loosely-bound EPS (L-EPS), and tightly-bound EPS (T-EPS), were extracted according to previous studies and were primarily composed of proteins, polysaccharides and humic acids (Fan et al., 2022).

The particle diameter was measured within a detection range of 0.02 to 2000 μm using a laser particle size analyzer. As the particle size gradually increased, sludge was sieved into several ranges, including 2.0–3.0 mm and 3.0–4.0 mm. XRD was used to analyze the inorganic composition of PDG. To reduce interference from organic matter, the samples were heated at 550 °C for 2 h (Fan et al., 2024b). XPS was used to evaluate element composition and valence, with data further processed using Avantage software. In addition, the composition of the PDG cores was detected using a Raman spectrometer (HORIBA JY LabRAM HR Evolution) with a laser wavelength of 532 nm.

2.7 High-throughput sequencing and metagenomic analysis

Samples from UCS-1 and UCS-2, consisting of granular and flocculated sludge during phase II-i and phase IV-ii, along with effluent sludge from phase IV-iii, were collected (Table S2) and subjected to freeze-drying to analyze microbial structure. DNA was extracted and then amplified by PCR with primers of 338F (5′-ACTCCTACGGGAGGCAGCA-3′) and 806R (5′-GGACTACHVGGGTWTCTAAT-3′). The normalized sequences underwent quality control, splicing, and were grouped into OTUs using a 97% identification thresholds. Raw sequence data had been archived in the NCBI database under Bioproject ID PRJNA1194738. Granular sludge from UCS-1 and UCS-2 in phase IV-ii was collected for metagenomic analysis, with raw data uploaded to the NCBI database under Bioproject ID PRJNA1195331. Detailed operation was described in Text S2.

3 Results and discussion

3.1 Impact of mechanical shear stress on nitrite production in continuous-flow reactors

3.1.1 Nitrite production in UCS-1

The UCS-1 was mainly operated under low-strength mechanical stirring with τ of 0.2–0.5 Pa (Fig. 1(c)). On day 13, NO_2^- accumulation was observed with an average NTR of 24.5% due to the recovery of denitrifying bacterial activity (Fig. 1(b)). In phase II, the τ was reduced to 0.2 Pa by adjusting the stirring intensity (Fig. 1(c)), alongside a gradual increase in influent NO_3^--N concentration from 63.2 (phase II-i) to 97.6 (phase II-ii), and 296.9 mg/L (phase II-iii). Correspondingly, NTR elevated from 44.0% to 46.4% and 55.5%, while the optimal COD/NO_3^--N ratio decreased from 3.5 to 2.5. These findings aligned with previous results observed in an SBR system (Fan et al., 2024b), where the use of electron donors facilitated the reduction of NO_3^- to NO_2^-, thereby decreasing the carbon demand for nitrite-to-nitrogen conversion.

Notably, in phase III-i, sludge flotation was observed when the NO_3^--N concentration reached 581.5 mg/L, resulting in severe sludge loss. This was accompanied by a significant decrease in NO_2^- accumulation, which could not be improved by elevating the τ to 0.9 and 1.1 Pa (Fig. 1(c)). In this case, τ was decreased to 0.2 Pa, with the influent NO_3^--N concentration decreasing from 581.5 (phase III-i) to 297.2 (phase III-ii), and 98.4 mg/L (phase III-iii). By employing this strategy, NO_2^- production was restored, and the average NO_2^--N concentration increased to 44.2 mg/L with an NTR of 48%.

In Phase IV, NO_3^--N concentration was further increased to 300.3 (phase IV-i), 587.9 (phase IV-ii), and 974.9 mg/L (phase IV-iii), with a τ of 0.5 Pa (Fig. 1(c)). Increasing NO_2^- accumulation was observed, with the NTR rising to 61.5%, 65.2%, and 72.5%. At an average NLR of 11.7 kg N/(m^3·d) and NO_3^--N concentration of 963 mg/L, UCS-1 achieved an NPR as high as 7.7 kg N/(m^3·d) (Fig. 1(a)). This was significantly higher than the values reported in previous studies in continuous-flow reactors, including NPR of 6.6 kg N/(m^3·d) achieved in a gas-circulated up-flow reactor (Cao et al., 2016), and NPR of 2.5 kg N/(m^3·d) obtained by increasing the up-flow liquid velocity through reducing HRT from 6.1 to 0.7 h (Li et al., 2022). These findings indicated that the ability to achieve higher NPR in continuous-flow reactors was closely related to the system's capacity to manage substrate overloading conditions. The occur-rence of substrate overloading could lead to sludge flotation and loss (Wang et al., 2018), consequently reducing NO_2^- accumulation.

3.1.2 Nitrite production in UCS-2

UCS-2 was mainly operated under high-strength mechanical stirring with τ of 1.2–1.4 Pa (Fig. 1(f)). In phase I, τ was controlled at 0.7 Pa, with an average NTR of 22.5% (Fig. 1(e)). In phase II, τ was increased to 1.2 Pa, and the influent NO_3^--N concentration remained consistent with that of UCS-1. This resulted in an increase in NTR from 37.1% (phase II-i) to 46.6% (phase II-ii) and 48.5% (phase II-iii), respectively (Fig. 1(e)). However, these values were still lower than those of UCS-1. It indicated that the continuous-flow system operated under low-strength τ was more conducive to NO_2^- accumulation when the influent NLR fluctuated. Furthermore, in phase II, the COD/NO_3^--N ratio in UCS-2 was notably higher than that in UCS-1, which led to a relatively lower NO_2^- production and higher effluent NO_3^--N concentration. This was mainly due to the enhanced competitive advantage of complete denitrifying bacteria in UCS-2 compared to UCS-1, thereby mitigating the NO_2^- accumulation.

To address the elevated effluent NO_3^--N concentration, HRT was extended from 2 to 3 h on day 106. Notably, prolonging HRT led to the complete denitrification, with a remarkable decrease in NTR from 56.5% to 0.6% (Fig. 1(e)). Consequently, HRT was reduced back to 2 h on day 114 to diminish the activity of complete denitrifying bacteria, leading to a rapid recovery of NO_2^- accumulation, with NTR increasing to 25.4%. These findings suggested that extending HRT in this continuous-flow system was detrimental to NO_2^- accumulation. To enhance the activity of functional bacteria, the influent NO_3^--N was raised to 581.5 mg/L, corresponding to an NLR of 7 kg N/(m^3·d) in phase III (Fig. 1(d)), while the τ increased from 1.4 to 1.6 Pa (Fig. 1(f)). However, under high loading conditions, a similar phenomenon to that observed in UCS-1 occurred: excessive sludge flotation accumulated at the outlet, hindering NO_2^- accumulation. Subsequently, when the influent NO_3^--N concentration was reduced, combined with lower τ, the performance of NO_2^- accumulation was significantly recovered, with an average NTR of 35.5%. These results demonstrated the importance of optimizing operational parameters, including HRT, τ, and influent NO_3^--N concentrations, to maximize NO_2^- accumulation and denitrification efficiency in continuous-flow systems.

In phase IV, the influent NO_3^--N concentration increased from 300.3 (phase IV-i) to 586.9 mg/L (phase IV-ii) under the τ of 1.4 Pa. This adjustment enhanced

NO_2^- accumulation, with the NTR increased to 62.2% (Fig. 1(e)). Notably, when the COD/NO_3^--N was increased from 2.3 to 2.5, the effluent NO_3^--N decreased by 40 mg/L, while the effluent NO_2^--N remained relatively stable. In contrast, in the UCS-1, the effluent NO_3^--N concentration decreased by 85.7 mg/L, accompanied by an increase of 58.9 mg/L in NO_2^--N concentration. This indicated that under high nitrogen loading and τ conditions, complete denitrifying bacteria outcompeted nitrite-accumulating bacteria, preferentially utilizing organic carbon for complete NO_3^- reduction. When the NO_3^--N concentration was further increased to 957.9 mg/L (phase IV-iii), the NO_2^- accumulation was disrupted (Fig. 1(e)). These findings indicated that lower-strength τ was more conducive to sustaining NO_2^- accumulation under high-loading conditions, as they mitigate the competitive advantage of complete denitrifiers over nitrite-accumulating bacteria.

3.2 Effect of shear stress on *ex-situ* microbial activity

The microbial activity of denitrifying bacteria in UCS-1 and UCS-2 exhibited distinct trends under varying operational conditions. During fluctuations in the NLR ranging from 0.4 to 7.1 kg N/(m^3·d), denitrifying microorganisms under the operation of low-strength τ (UCS-1) exhibited higher r_{NO_2} and r_{NO_3} in both granules (Fig. 2(a)) and flocs (Fig. 2(b)) compared to high-strength τ (UCS-2), indicating that low-strength τ conditions tended to promote microbial activity in continuous-flow systems.

Notably, under the fluctuation of NLR, r_{NO_2} and r_{NO_3} of flocculated sludge in the two systems were significantly higher than those of granular sludge (Fig. 2(b)). With influent NLR of 7.1 kg N/(m^3·d) in UCS-1, r_{NO_2} and r_{NO_3} of flocculated sludge were 286.7 and 344.7 mg/(gVSS·h), obviously higher than 79.1 and 178.1 mg/(gVSS·h) observed of granular sludge in UCS-1, respectively. Similarly, in UCS-2, r_{NO_2} and r_{NO_3} of flocculated sludge were notably higher than granular sludge. Specifically, r_{NO_2} and r_{NO_3} of flocculated sludge reached 270.4 and 318.6 mg/(gVSS·h), respectively, while the corresponding values for granular sludge were 77.4 and 155.6 mg/(gVSS·h). These findings indicated that flocculated sludge played a key role in promoting NO_2^- accumulation in continuous-flow systems.

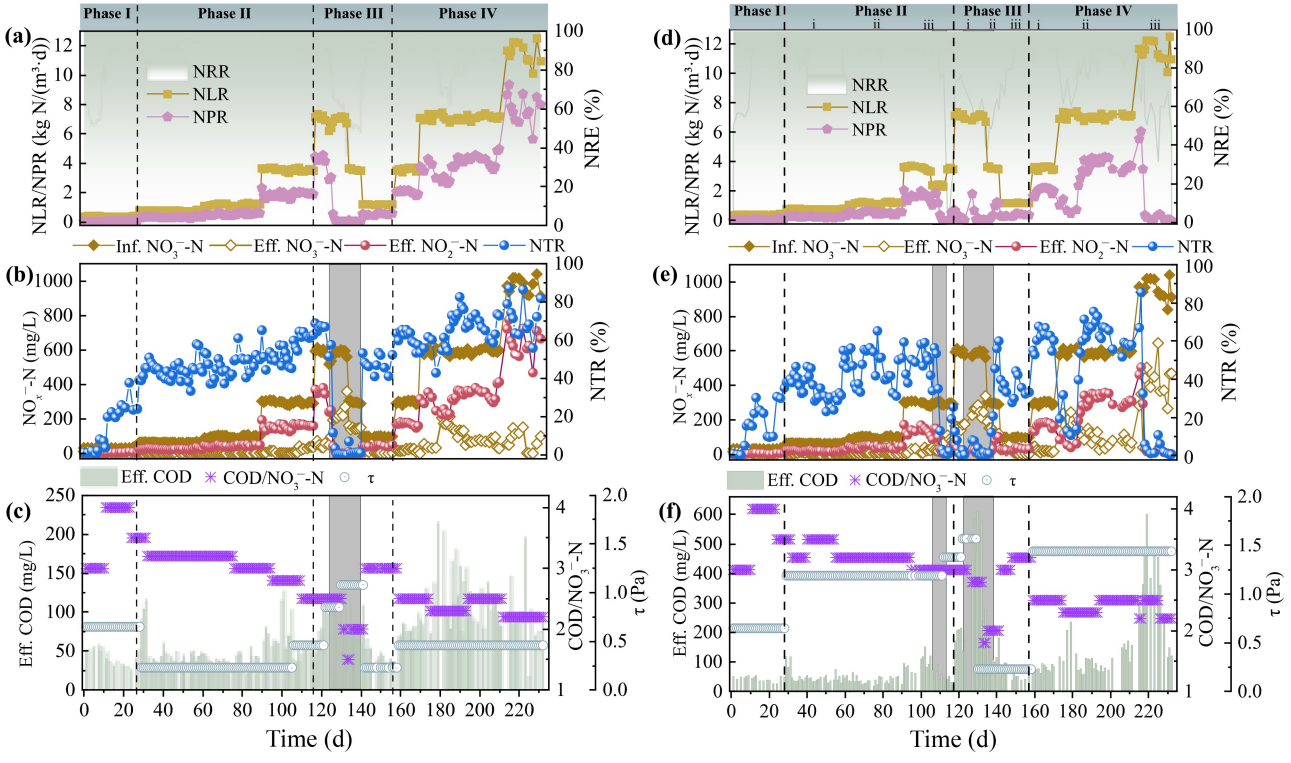

Fig. 1 Operational parameter in UCS-1 and UCS-2, including (a) and (d) variation in NLR, NPR, and NRE; (b) and (e) Inf. NO_3^--N, Eff. NO_3^--N, Eff. NO_2^--N, and NTR; (c) and (f) Eff. COD, COD/NO_3^--N, and τ. (The gray shaded parts represent the disruption of nitrite accumulation).

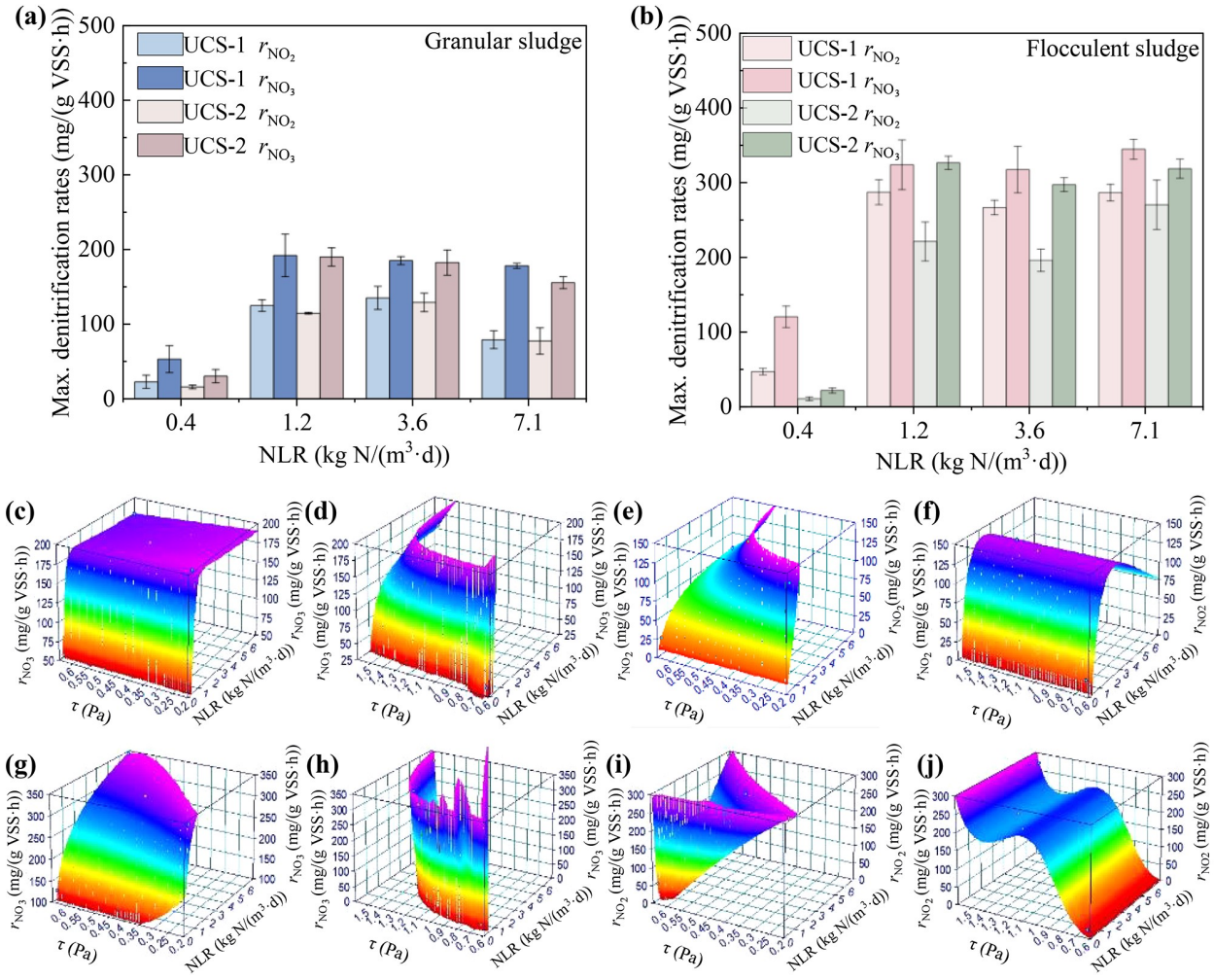

Fig. 2 The variation in the activity of functional bacterial communities under different NLRs in (a) granular sludge and (b) flocculent sludge, and the three-dimensional nonlinear fitting relationship between NLR, shear stress (τ), and max. denitrification rates in granular sludge including r_{NO3} in (c) UCS-1 and (d) UCS-2 and r_{NO_2} in (e) UCS-1 and (f) UCS-2, and flocculent sludge including r_{NO_3} in (g) UCS-1 and (h) UCS-2 and r_{NO_2} in (i) UCS-1 and (j) UCS-2.

In addition, an excellent nonlinear fit relationship among τ, NLR, and maximum denitrification rates (r_{NO_2} and r_{NO_3}) was shown in Figs. 2(c)–2(j). For granular sludge, r_{NO_2} and r_{NO_3} were closely related to NLR, consistent with previous findings in SBR systems that demonstrated an improvement in specific denitrification activity with increasing influent NO_3^--N concentration, thereby enhancing the conversion rate of NO_3^- to NO_2^- (Fan et al., 2022). For flocculated sludge, τ mainly affected the r_{NO_2} of UCS-2 (Fig. 2(j)), and NLR and τ were the key factors affecting the r_{NO_2} and r_{NO_3} of UCS-1 (Fig. 2(i)). These above findings suggested that τ and NLR played a predominant role in enhancing maximum denitrification rates, and it was expected to increase NO_2^--N accumulation in continuous-flow systems by meticulously regulating the influent NLR and τ.

3.3 Effect of mechanical shear stress on the PD sludge granulation

Mechanical shear stress had a significantly distinct effect on the distribution of granules (Fig. S2). In UCS-1, granules of 1 mm ⩽ d < 2 mm were gradually enriched under the τ of 0.2–0.5 Pa (Fig. S2(a)), accounting for the highest proportion of 50.3% on day 194 (Fig. S2(c)). Larger granules (d > 2mm) decreased from 28.3% on day 194 to 2% on day 232 (Fig. S2(c)), likely due to the flotation and discharge of oversized granules. Differentially, in UCS-2, PDG of 1 mm ⩽ d < 2 mm progressively disintegrated during phase I and phase II (Fig. S2(d)). The disintegration possibly resulted from the granular sludge's inability to adapt to the high-strength τ, leading to enhanced collision frequency

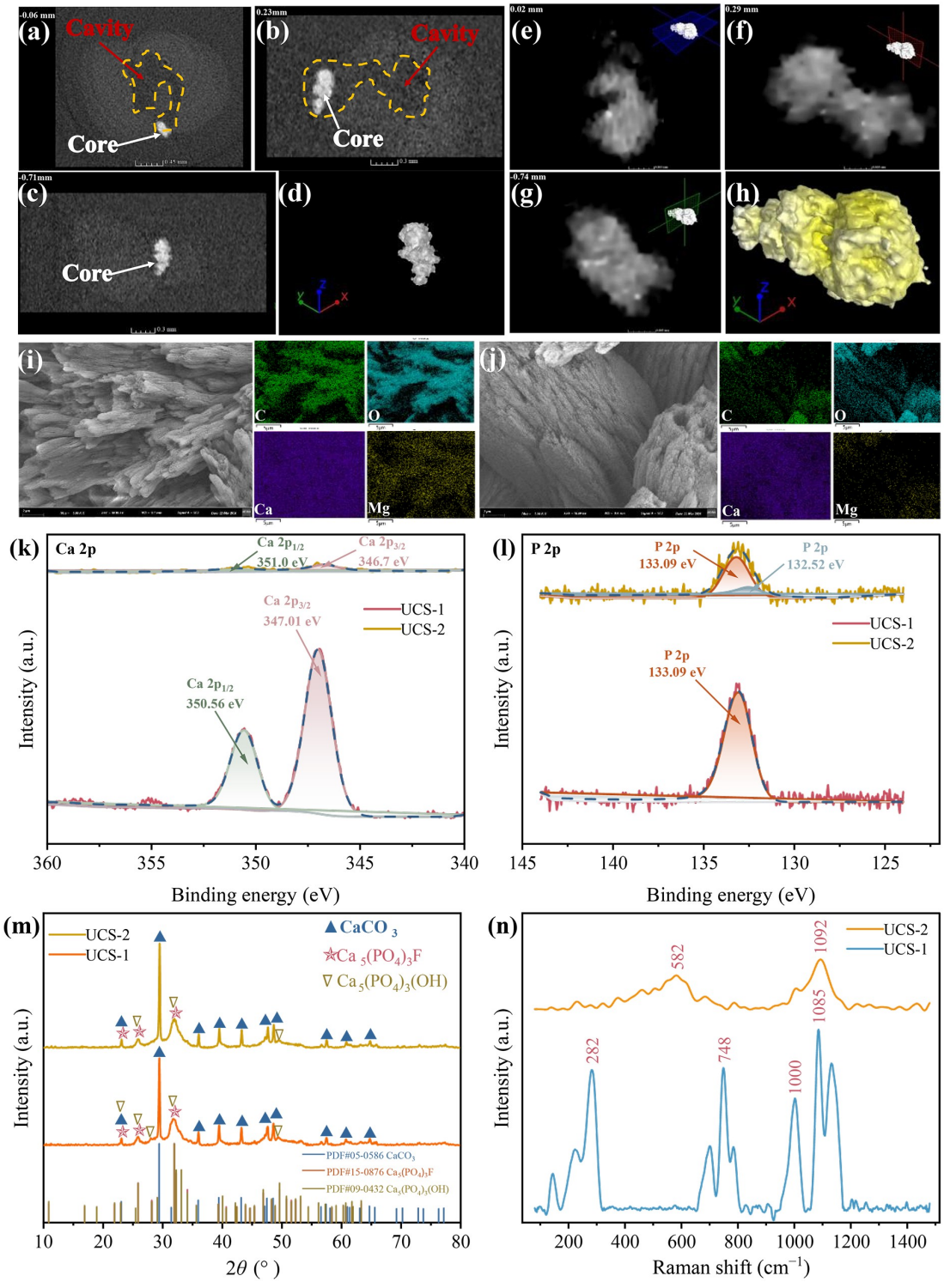

Fig. 3 Micro-CT Observation of a granular sludge. The two-dimensional cross-section slices of granular sludge were based on (a) *x-y* axis plane, (b) *y-z* axis plane, and (c) *x-z* axis plane. (d) three-dimensional diagram of the inorganic core. The two-dimensional cross-section slices of inorganic core in granular sludge were based on (e) *x-y* axis plane, (f) *y-z* axis plane, and (g) *x-z* axis plane. (h) three-dimensional diagram of the inorganic core based on different densities. The SEM images of the inorganic core and energy dispersive spectrometer in (i) UCS-1 and (j) UCS-2, respectively. XPS analysis based on element (k) Ca, (l) P, and (m) XRD analysis and (n) Raman analysis of UCS-1 and UCS-2.

among the larger particles. However, during phase IV, granules of 1 mm ⩽ d < 2 mm reached their peak under high-strength shear conditions (τ = 1.4 Pa), varying between 39.1% and 49.7% (Fig. S2(f)). Notably, granules larger than 2 mm increased substantially, from 35.6% on day 194 to 66.0% on day 232. Correspondingly, the extracellular polymeric substances (EPS) content also exhibited an upward trend in phase IV, increasing from 193.7 mg/g VSS in phase IV-i to 358.8 mg/g VSS in phase IV-ii at the τ of 1.4 Pa (Fig. S3). This observation aligns with previous studies that high-strength τ promoted EPS secretion, facilitating the capture of microorganisms through the physical and chemical interactions, thereby leading to an increase in the particle size of the granular sludge (Wang et al., 2022; Liu et al., 2023).

These findings indicated that mechanical shear stress played a pivotal role in shaping PDG size distribution under fluctuating influent NLR conditions. Low-strength τ favored the maintenance of cohesive granules, while high-strength τ first promoted granule fragmentation, and then enriched granules of d > 2 mm. This shift altered the balance between granular and flocculated sludge, thereby influencing the overall stability and functionality of the system.

3.4 Internal nucleus properties and compositions of PDG

3.4.1 Morphological features of the internal nucleus

The internal structure of PDG was conducted for micro-CT analysis. Spatial regions within the PDG were segmented based on structural density variations. Dark gray areas in the micro-CT images represented low-density and porous regions (Figs. 3(a)–3(c)), indicating the presence of internal cavities. These cavities were hypothesized to result from gas production during biological processes, including carbon dioxide (CO_2) from the decomposition of sodium acetate, and nitric oxide (NO), nitrous oxide (N_2O), and N_2 generated during denitrification (Fan et al., 2024b). The accumulation of these gases likely increased internal pressure, causing expansion and pore formation. This structural adaptation suggested that gas dynamics within PDG significantly influenced its morphology and stability.

In contrast, white areas in the micro-CT images represented regions with higher mineralization density. Three-dimensional visualization of these regions (Fig. 3(d)) revealed irregularly shaped mineralized cores with numerous surface pits. These cores were hypothesized to act as nucleation sites that facilitated the aggregation and structural stabilization of granular sludge. Two-dimensional slice analysis of samples from different planes revealed that the core was relatively compact and denser (Figs. 3(e)–3(g)), exhibiting greater aggregation compared to previously reported nitrifying granular sludge, where hydroxyapatite ($Ca_5(PO_4)_3(OH)$) served as the core (Guo et al., 2021). This finding highlighted the distinct mineralization processes driving PDG formation and stability. Further three-dimensional imaging of the PDG core revealed heterogeneity in core composition, primarily comprising light yellow and light white substances (Fig. 3(h)) (The video of the three-dimensional structure of the PDG core is available in the supplementary materials). These differences in density and composition underscored the critical role of mineralized cores in maintaining PDG integrity in denitrification with high NO_2^- accumulation. Collectively, these observations provided a mechanistic understanding of the structural development of PDG, emphasizing the interplay between mechanical shear stress, gas production, pore formation, and mineralized core establishment as key factors underpinning the formation and resilience of granular sludge in denitrification systems.

Cross-sectional SEM observations of the core from both UCS-1 and UCS-2 revealed a layered and relatively compact structure (Figs. 3(i) and 3(j)). Elemental analysis of the core surface indicated that calcium (Ca) was the predominant element, constituting 44.9% in UCS-1 and 59.7% in UCS-2. Oxygen (O) and carbon (C) were the next most abundant elements, accounting for 40.4% and 11.4% in UCS-1, and 32.2% and 7.7% in UCS-2, respectively (Table S3). These findings strongly suggested that the core was primarily composed of calcium-containing compounds, which likely contributed to its compactness and structural stability in forming and maintaining the core structure.

3.4.2 Chemical composition of the inorganic nucleus

The inorganic composition of PDG under two different shear stresses was further analyzed. XPS results showed that the proportions of calcium (Ca) and phosphorus (P) in UCS-1 were higher than those in UCS-2, with these elements predominantly present as calcium carbonate ($CaCO_3$) and hydroxyapatite ($Ca_5(PO_4)_3(OH)$), which were the dominant components of the inorganic nucleus. Specifically, the binding energy peaks of Ca $2p_{3/2}$ (346.7 and 347.01 eV) and Ca $2p_{1/2}$ (350.56 and 351.0 eV) confirmed the presence of $CaCO_3$ (Kiehl et al., 2013) (Fig. 3(k)). Similarly, the P 2p binding energies (133.09 and 132.52 eV) were consistent with the presence of $Ca_5(PO_4)_3(OH)$ (Majjane et al., 2014)

(Fig. 3(l)). These findings indicated that the inorganic core composition of PDG was largely governed by calcium-based compounds, regardless of the τ.

XRD analysis corroborated the XPS results, identifying $CaCO_3$ as the predominant inorganic component of PDG, followed by $Ca_5(PO_4)_3F$ and $Ca_5(PO_4)_3(OH)$ (Fig. 3(m)). This composition was consistent with previous studies on SBR systems (Fan et al., 2024b) and suggested that variations in mechanical stirring intensity in a continuous-flow system did not significantly alter the fundamental inorganic makeup of PDG. These results highlighted the robust nature of the core formation mechanism in PDG across different operational conditions.

Raman spectroscopy further confirmed the significant absorption peaks for $CaCO_3$ at ~282 and ~1085 cm^{-1} (Černý et al., 2004), and for $Ca_5(PO_4)_3(OH)$ at 582 cm^{-1} (Fig. 3(n)) (Angela et al., 2011). Notably, the signal intensity of $CaCO_3$ was markedly higher in UCS-1 than in UCS-2, indicating that low-strength τ enhanced the formation of granules with $CaCO_3$-dominated cores. Additionally, a peak at ~748 cm^{-1} was identified as tryptophan, which contained hydrophobic groups that promoted microbial adhesion and aggregation (Cui et al., 2022). This provided a mechanistic explanation for the enhanced formation of PDG under low-strength τ conditions. Collectively, these findings suggested that low-strength τ not only favored the enrichment of $CaCO_3$ but also supported biochemical factors that enhanced granule formation and stability in continuous-flow systems.

3.5 Shear stress-driven microbial community dynamics in PD under varying NLR

3.5.1 Structure succession of functional microorganisms

To understand shear stress-induced variations in microbial community structure, 16S rRNA gene amplicon sequencing was performed across operational phases (Fig. 4). Principal component analysis (PCA) revealed a distinct separation between U1_1 (τ = 0.2 Pa) and U2_1 (τ = 1.2 Pa) during initial operation, confirming τ as a primary driver of initial-phase community differentiation (Fig. 4(a)). However, progressive increase in NLR (0.8–7.1 kg N/(m^3·d) in UCS-1 and UCS-2) and τ (0.2–0.5 Pa in UCS-1, 1.2–1.4 Pa in UCS-2) drove convergent clustering of granular and flocculated sludge communities in both systems. These findings demonstrated that while shear stress intensity initially impacted the microbial community differentiation, sustained co-elevation of NLR and τ selected for convergence of dominant taxa, reflecting the microbial adaptability to operational conditions in PD systems.

At the genus level, *Thauera*, a member of the *Proteobacteria*, was the most abundant and recognized for its role in high NO_2^- production (Du et al., 2019; Fan et al., 2022). Significantly, with the increase in τ and under fluctuating NLR, the relative abundance of *Thauera* in UCS-1 remarkably rose in granular sludge (4.6% → 57.1%) and flocculated sludge (0% → 64.7%) (Fig. 4(b)). Similarly, in UCS-2, *Thauera* increased in granular sludge (41.1% → 70.7%) and flocculated sludge (1.7% → 69%). Notably, *Thauera* exhibited faster growth in flocculated sludge, which was likely relevant to higher r_{NO_2} and r_{NO_3} described in Fig. 2(b). Furthermore, *Thauera* was the dominant microbial group in the effluent sludge during phase IV-iii, comprising 54.1% in UCS-1 and 86% in UCS-2 (Fig. S4), which was likely a key factor contributing to the sudden reduction in NO_2^- production in UCS-2 under high-strength τ.

In contrast, *Dechloromonas*, also a member of *Proteobacteria* and known for its metabolic capacities for carbon storage and heterotrophic denitrification (He et al., 2021), was initially abundant in granular and flocculent sludge but gradually declined. This suggested that *Thauera* outcompeted *Dechloromonas* under high NLR and elevated τ conditions. Conversely, *Aquimonas*, another denitrifying bacterium from *Proteobacteria*, could degrade organic carbon (Ma et al., 2023), showed an increasing trend in UCS-1 (0.5%–6.8% in granular sludge, 1.9%–3.5% in flocculated sludge) and UCS-2 (0.3%–6.6% in granular sludge, 4.1%–4.6% in flocculated sludge). These results suggested that microbial community structure exhibited distinct adaptive responses to the varying NLR and τ conditions.

3.5.2 Co-occurrence network analysis of functional microorganisms

To unravel the regulatory effects of NLR, τ, and COD/NO_3^--N on microbial structure, the molecular ecological network analysis was employed using the top 50 genera (Pearson: $R \geqslant 0.5$, $p < 0.05$). The low-strength τ system (UCS-1) exhibited a microbial network with 13 nodes, 23 edges, and an average degree of 3.538 (Fig. 4(c)), which was lower than the high-strength τ system (UCS-2), with 14 nodes, 27 edges, and an average degree of 3.857 (Fig. 4(d)). This indicated that microbial community interactions became more complex under the high-strength τ.

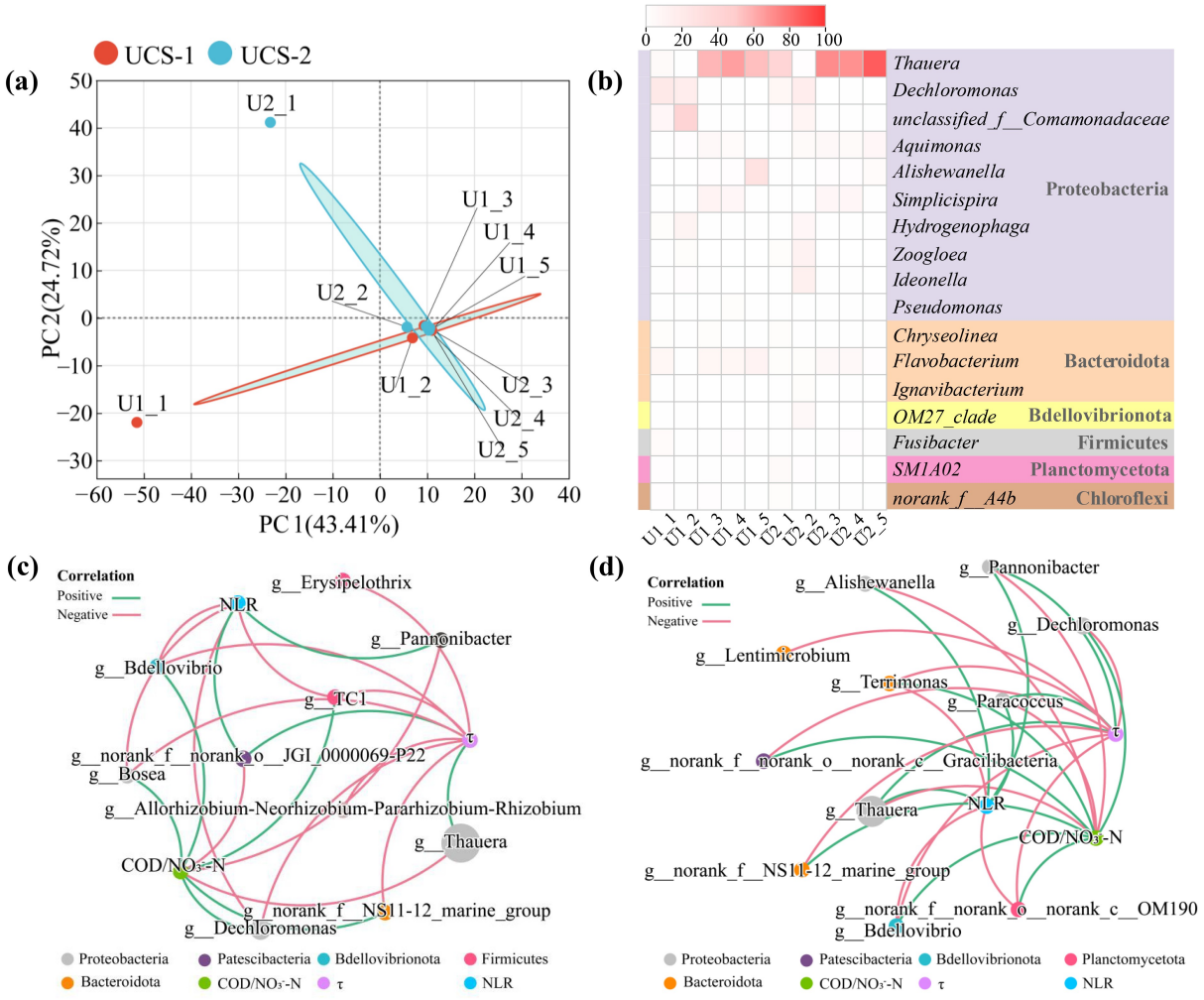

Fig. 4 Microbial structure of the UCS-1 and UCS-2. (a) PCA analysis on the OTU level. (b) Microbial composition at the genus level. The molecular ecological network analysis of genus and influence factor in (c) UCS-1 and (d) UCS-2.

Specifically, in UCS-2, *Thauera* showed positive correlations with both NLR (R = 0.89, p < 0.01) and τ (R = 0.89, p < 0.01), while exhibiting a negative correlation with COD/NO_3^--N. Conversely, in UCS-1, the proportion of *Thauera* was strongly correlated with τ (R = 0.99, p < 0.01) but negatively correlated with COD/NO_3^--N. *Dechloromonas* exhibited positive correlations with COD/NO_3^--N in both systems (UCS-1: R = 0.95, p < 0.01; UCS-2: R = 0.88, p < 0.01), consistent with previous study that *Dechloromonas* was enriched under high COD/NO_3^--N conditions (Chen et al., 2023).

The above results indicated that elevated τ in both UCS-1 and UCS-2 promoted the growth of *Thauera* under varying NLR. A combination of high-strength τ and high NLR emerged as optimal conditions for the enrichment of *Thauera*, underscoring its adaptability and competitive advantage in denitrifying systems.

3.6 Metagenomics insight into shear stress-driven nitrogen-carbon metabolic coordination

3.6.1 Response of τ to functional gene abundance and metabolic pathway

To elucidate the nitrogen and carbon metabolism mechanisms in granular sludge, metagenomic analysis was performed on phase IV-ii samples from UCS-1 (τ = 0.5 Pa) and UCS-2 (τ = 1.4 Pa). In this study, nitrogen metabolism was primarily driven by the denitrification pathway, while carbon metabolism centered around acetate metabolism. Specifically, acetyl-CoA generated during acetate metabolism served as a pivotal intermediate and can either enter the tricarboxylic acid (TCA) cycle to generate NADH and $FADH_2$, or be directed toward the biosynthesis of poly-β-hydroxybutyrate (PHB) (Zhang et al., 2021). Moreover, organic

compounds generated by systemic metabolism can also be converted into acetyl-CoA via the pyruvate pathway.

The impact of τ on the abundance variation of key functional genes involved in nitrogen and carbon metabolism was investigated. Compared to high-strength τ, low-strength τ led to a significantly higher abundance of nitrate reductase genes (*napAB* and *narGHI*), nitrite reductase genes (*nirKS*), and nitric oxide reductase gene (*nosZ*) (Fig. 5(a)). In carbon metabolism, the *pdhABCD* genes were involved in the production of NADH during the conversion of pyruvate to acetyl-CoA (Soriano-Baguet et al., 2023), which exhibited substantially greater abundance in low-strength τ (2366.5) compared to the high-strength τ (2189.6) (Fig. 5(b)). Concurrently, a higher abundance of TCA cycle-associated NADH-generating genes (*mdh*, *IDH13*, *korABCD*) and $FADH_2$-linked *sdhABCD* genes was observed under low-strength τ, ensuring robust electron generation.

Functional microbial contributions to nitrogen and carbon metabolism genes were further discussed under the two different τ (Fig. 5(c)). *Thauera* showed a substantial influence on denitrification genes, with higher contributions to NO_3^- reductase and NO_2^- reductase under high-strength τ, likely attributed to its higher relative abundance. Moreover, *Thauera* emerged as the primary contributor to carbon metabolism, especially under high-strength τ, which promoted regulatory contributions related to pyruvate metabolism and the TCA cycle, facilitating sufficient electron transfer within the electron transport chain. Conversely, *Dechloromonas* showed negligible contributions due to its lower proportion (< 0.01%) under the high-strength τ.

These findings indicated that low-strength τ was more conducive to promoting the synergistic nitrogen and carbon metabolism in the granular sludge system, whereas high-strength τ enhanced the contribution of the dominant bacteria *Thauera* to the nitrogen and carbon metabolism.

3.6.2 Response of τ to intraspecific relationship within *Thauera* consortia

The effect of τ on the relative abundance of *Thauera* species and their contributions to key nitrogen-carbon metabolism genes was investigated. *Thauera*_sp., as the dominant species (53.4% in UCS-1 and 56.1% in UCS-2) (Fig. 6(a)), showed varying gene contribution patterns under different τ conditions. Compared to low-strength τ, *Thauera*_sp. showed a 3.6% decrease in the *napA* gene contribution, while its contribution to *nirK* and *nosZ* genes increased by 3.7% and 11.2%, respectively, under the high-strength τ (Fig. 6(b)). This indicated a metabolic shift towards complete denitrification, explaining the reduced NO_2^- accumulation in phase IV-iii. In acetate metabolism, the conversion of acetate to acetyl-CoA was mediated by two distinct metabolic pathways, including the ATP-dependent acs-encoded synthesis pathway and the ATP-independent ackA-pta synthesis pathway (Kumari et al., 1995). *Thauera*_sp. primarily relied on the acs-encoded synthesis pathway, contributing 73.1% in UCS-1 and 82.8% in UCS-2, higher than that ackA-pta pathway (4.2%–23.1% in UCS-1, 7.7%–32.3% in UCS-2) (Fig. 6(b)). Additionally, its contribution to *pdhABCD*, *korAB*, and *sdhABCD* genes increased under the high-strength τ.

In contrast, *Thauera*_phenylacetica (27.9% in UCS-1 and 22.5% in UCS-2) contributed more to *napA* than to *nirK* (26.4% vs 13% in UCS-1, 23.4% vs 9.3% in UCS-2), and primarily synthesized acetyl-CoA via the ackA-pta pathway, with contribution rates of 59.2%–76.8% in UCS-1 and 43.3%–67.7% in UCS-2, higher than the *acs* gene (0% in UCS-1 and UCS-2). Notably, *Thauera*_phenylacetica, as the only strain in *Thauera* in this study, was capable of encoding the *cs* gene, which regulated the entry of acetyl-CoA into the TCA cycle, and showed a relatively high contribution to nitrogen-carbon genes under the low-strength τ. Moreover, *Thauera*_sp._WB-2 contributed to *napA* (15.4% in UCS-1, 22% in UCS-2) higher than to *nirKS* (0% in UCS-1 and UCS-2), suggesting its pivotal role in promoting NO_2^- accumulation under high-strength τ.

These results indicated that τ induced intraspecific metabolic regulation strategies within the *Thauera* consortia. Under low-strength τ, *Thauera*_phenylacetica and *Thauera*.sp. likely collaborated through the ackA-pta and acs pathways, respectively, to promote electron generation and facilitate NO_2^- accumulation. Conversely, under high-strength τ, *Thauera*.sp. predominated in acetate metabolism via the acs pathway, driving complete denitrification.

3.7 Mechanism of granules formation under the varying mechanical shear stresses

To visually elucidate the impact of varying shear stresses on the spatial distribution of PD sludge and the aggregation process of granules within continuous-flow systems, this study presented a comprehensive analysis of the granule formation mechanisms and electron transfer pathways within carbon-nitrogen metabolic processes from both macroscopic and microscopic perspectives (Fig. 7).

At the macroscopic level, granules under low-

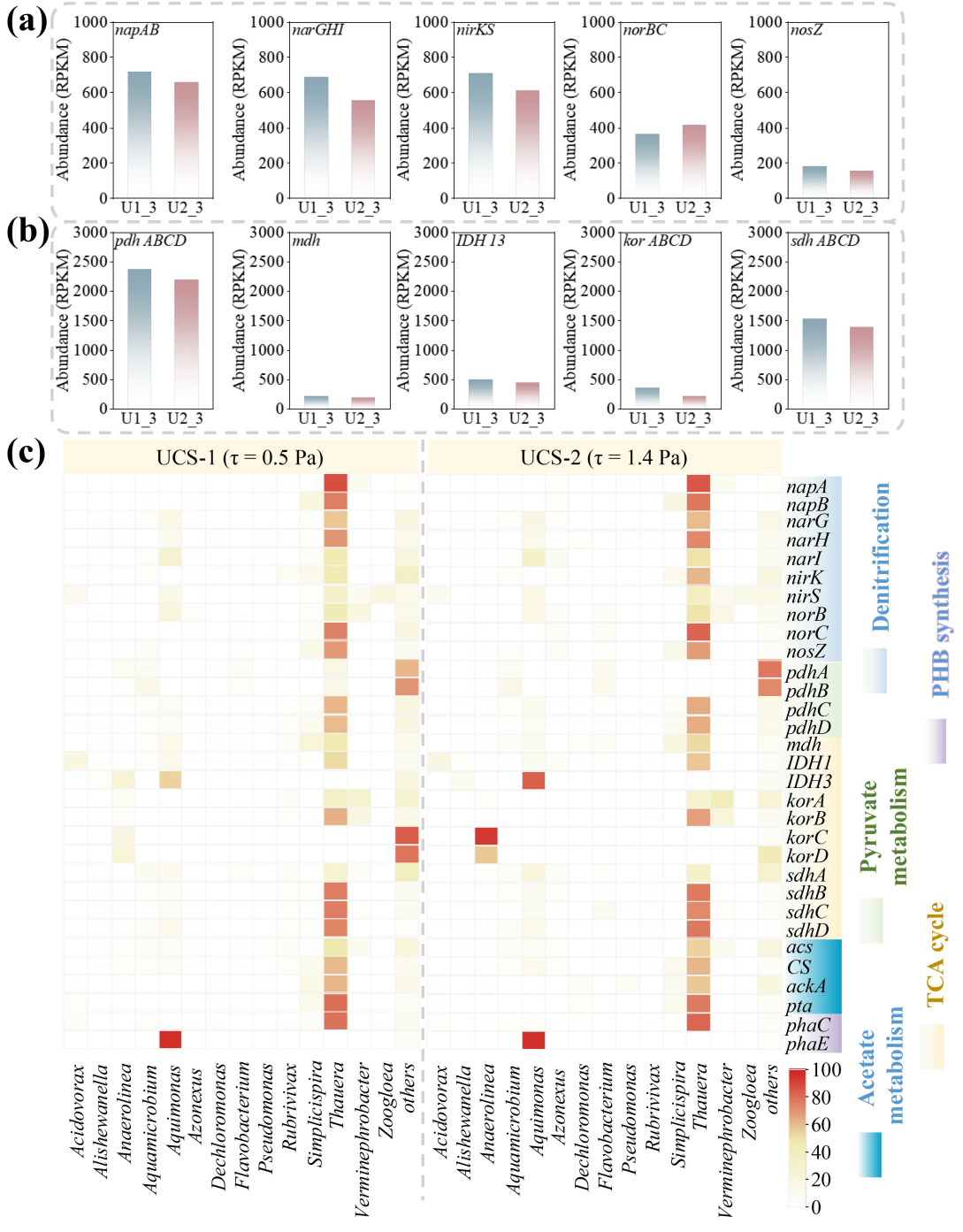

Fig. 5 Metagenomic analysis of the granular sludge in UCS-1 and UCS-2 on phase IV-ii. The abundance values of (a) denitrification-related genes and (b) genes associated with energy production in carbon metabolism. (c) Taxonomic origins of the key enzymes in nitrogen metabolism at the genus level. (The colors of the heatmap represented the contribution ratio of the genus to genes, calculated using RPKM).

strength τ predominantly aggregated at the bottom of the reactor, with the granules sizes mainly ranging from 1 to 2 mm, facilitating substrate absorbing, while flocculated sludge largely adhered to the reactor walls (Fig. S2(a) and S2(c)). Conversely, under high-strength τ, granules were more evenly distributed, enabling uniform substrate uptake. Large granules initially disintegrated into smaller particles and flocculated

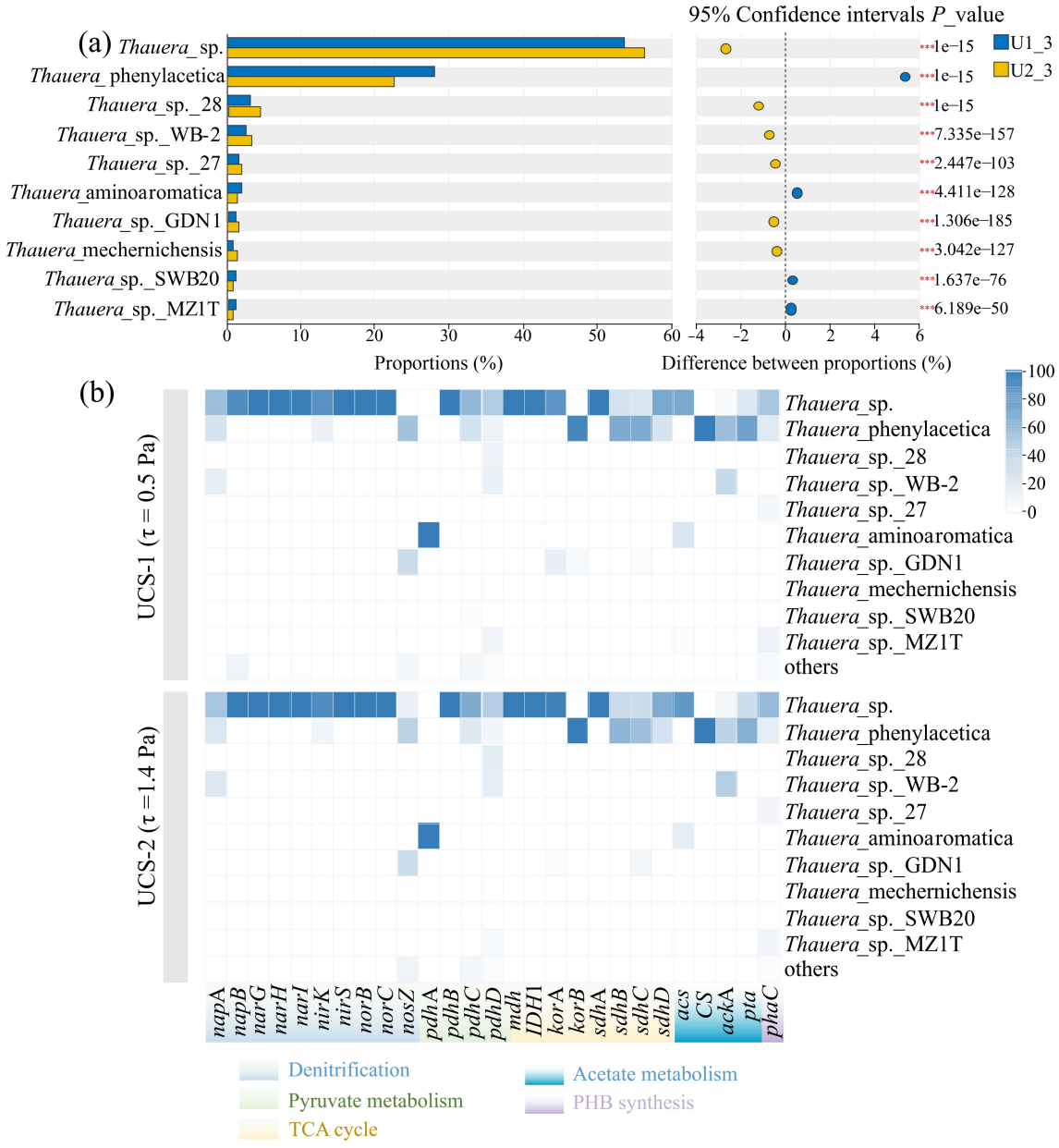

Fig. 6 (a) The relative abundance of *Thauera* at the species level. (b) Taxonomic origins of the key enzymes involved in nitrogen and carbon metabolism at the *Thauera* species level. (The colors of the heatmap represented the contribution ratio of *Thauera* species to genes, calculated using RPKM).

sludge due to intensified mixing, which reduced wall adhesion and further facilitated the formation of 2–4 mm granules. τ from mechanical stirring and the rotation of granules promoted enhanced flow between flocculated sludge and substrates, leading to preferential substrate uptake. This may explain the higher enrichment of *Thauera* and elevated denitrification rates in flocculated sludge compared to granules.

At the microscopic level, τ modulated the selective expression of functional genes. Low-strength τ facilitated synergistic nitrogen-carbon metabolism, resulting in significantly higher abundances of NO_3^- and NO_2^- reductase genes compared to high-strength τ. This metabolic advantage was attributed to improved electron transfer efficiency under low-strength τ, which accelerated the conversion of NO_3^- to NO_2^-.

3.8 Practic implications

This study demonstrated that τ generated by mechanical

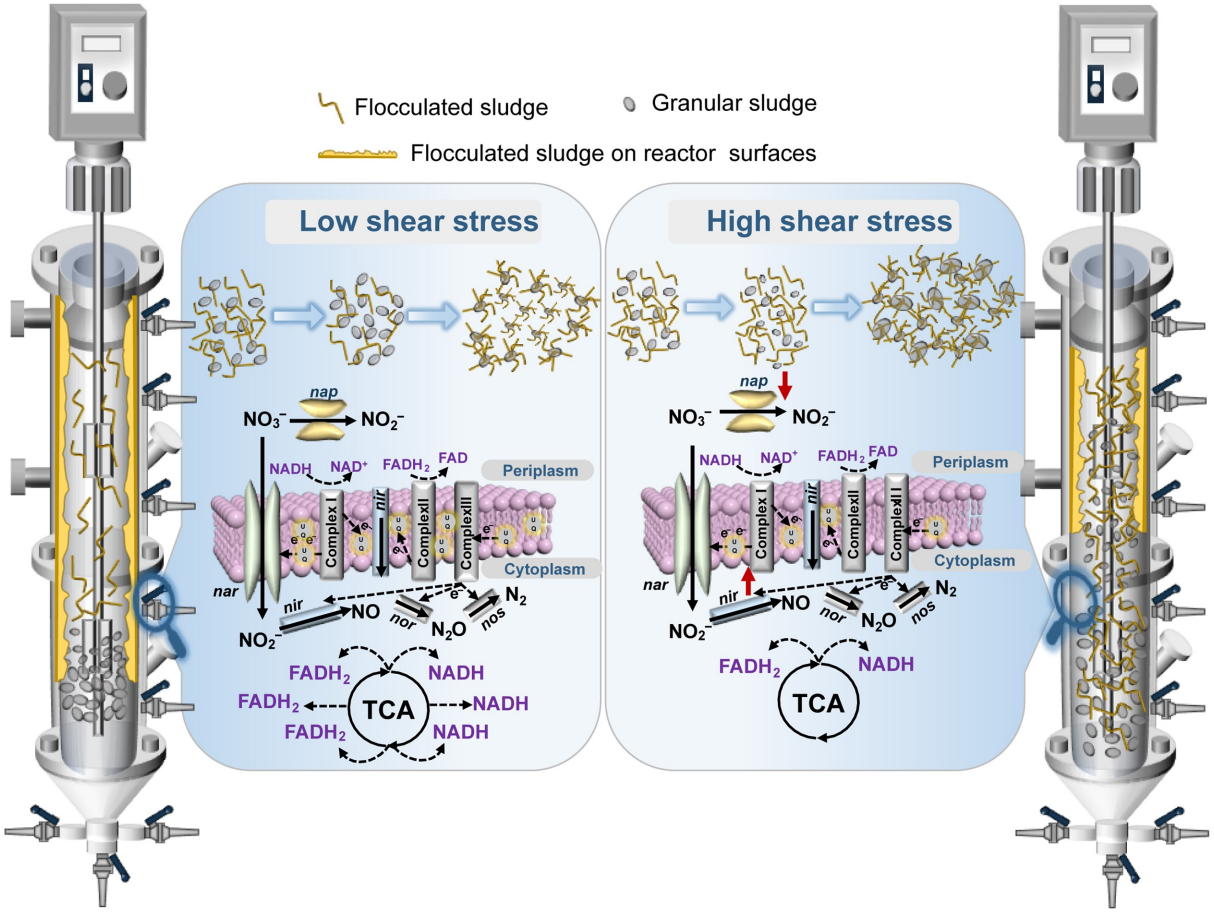

Fig. 7 The proposed mechanism of granular sludge formation driven by mechanical mixing under low (UCS-1) and high (UCS-2) shear stress.

stirring can effectively enhance sludge mass transfer and promote the formation of PDG with high nitrite production. PDG exhibited excellent settling performance, resilience to shock loads, and tolerance to environmental fluctuations (Xu et al., 2023), making it an ideal nitrite supplier for anammox processes aimed at treating wastewater containing nitrate (e.g., pharmaceutical wastewater, metal pickling effluent) and ammonia (e.g., domestic sewage, digestion) (Zhang et al., 2022; Qin et al., 2024).

In this study, τ and NLR were identified as the critical operational parameters influencing PDG performance. Compared to the high-strength τ (1.2–1.4 Pa), low-strength τ (0.2–0.5 Pa) maintained the structural stability of PDG and achieved an NPR of 7.7 kg N/(m^3·d) at an NLR of 11.7 kg N/(m^3·d). Additionally, a rapid increase in NLR triggered sludge flotation, regardless of whether τ was low or high. This suggested that a moderate increase in influent NLR was essential for enhancing system adaptability in practical operations.

To improve the operational stability of PDG in engineering applications, incorporating a regulation tank at the inlet can homogenize influent water quality, thereby reducing the adverse impacts on PDG. A secondary sedimentation tank installed at the outlet, combined with sludge recirculation, can retain biomass concentration. Furthermore, actual wastewater often contains insufficient biodegradable organic carbon, which limits the nitrite production. Therefore, the external addition of readily biodegradable carbon sources (e.g., sodium acetate) is essential to sustain a stable nitrite supply for the anammox process and ensure efficient nitrogen removal.

4 Conclusions

This study highlighted the crucial role of mechanical shear stress as a pivotal engineering parameter in modulating the formation and structure of granular

sludge, as well as the metabolic regulation within the dominant *Thauera* species, which provided new insights into optimizing operational strategies for enhancing NO_2^- accumulation in continuous-flow denitrification systems. By regulating low-strength τ (0.2–0.5 Pa), the formation of dense and substrate-absorbing granules with $CaCO_3$-dominated cores was promoted, leading to increased electron generation and higher abundance of key enzymes involved in nitrogen-carbon metabolism, along with enhanced microbial activity. Moreover, under low-strength τ, gradually reducing the influent NO_3^- concentration in a continuous-flow system facilitated the restoration of NO_2^- accumulation. Conversely, high-strength τ (1.2–1.4 Pa) promoted the uniform distribution of granules, reduced wall adhesion, and enhanced homogeneous substrate interaction and granule formation. This promoted the enrichment of *Thauera*, however, it led to a decreased contribution of *Thauera*.sp. to *napA* and an increased contribution to *nirK*, thereby hindering NO_2^- accumulation.

Conflicts of Interest Rui Du is a youth editorial board member and Yongzhen Peng is an advisory board member of *ENGINEERING Environment*. The authors declare that the research was conducted in the absence of any commercial or financial relationships that could be construed as a potential conflict of interest.

Acknowledgements This study was funded by the National Natural Science Foundation of China (No. 52470023) and Beijing Nova Program, China (No. 20240484634).

Electronic Supplementary Material Supplementary material is available in the online version of this article at https://dx.doi.org/10.1007/s11783-026-2154-4 and is accessible for authorized users.

References

Al-Hazmi H E, Maktabifard M, Grubba D, Majtacz J, Hassan G K, Lu X, Piechota G, Mannina G, Bott C B, Mąkinia J (2023). An advanced synergy of partial denitrification-anammox for optimizing nitrogen removal from wastewater: a review. Bioresource Technology, 381: 129168

Angela M, Béatrice B, Mathieu S (2011). Biologically induced phosphorus precipitation in aerobic granular sludge process. Water Research, 45(12): 3776–3786

Bode H, Seyfried C F, Kraft A (1987). High-rate denitrification of concentrated nitrate wastewater. Water Science and Technology, 19(1−2): 163–174

Cao S B, Du R, Zhou Y (2021). Coupling anammox with heterotrophic denitrification for enhanced nitrogen removal: a review. Critical Reviews in Environmental Science and Technology, 51(19): 2260–2293

Cao S B, Li B K, Du R, Ren N Q, Peng Y Z (2016). Nitrite production in a partial denitrifying upflow sludge bed (USB) reactor equipped with gas automatic circulation (GAC). Water Research, 90: 309–316

CŒrný P, JelíNková H, Zverev P G, Basiev T T (2004). Solid state lasers with Raman frequency conversion. Progress in Quantum Electronics, 28(2): 113–143

Chen G J, Lin L, Wang Y, Zhang Z K, Cao W Z, Zhang Y L (2023). Unveiling the interaction mechanisms of key functional microorganisms in the partial denitrification-anammox process induced by COD. Frontiers of Environmental Science & Engineering, 17(8): 103

Cui D Y, Kong L C, Wang Y, Zhu Y Q, Zhang C L (2022). *In situ* identification of environmental microorganisms with Raman spectroscopy. Environmental Science and Ecotechnology, 11: 100187

Du R, Cao S B, Li B K, Niu M, Wang S Y, Peng Y Z (2017). Performance and microbial community analysis of a novel DEAMOX based on partial-denitrification and anammox treating ammonia and nitrate wastewaters. Water Research, 108: 46–56

Du R, Peng Y Z, Ji J T, Shi L L, Gao R T, Li X C (2019). Partial denitrification providing nitrite: opportunities of extending application for anammox. Environment International, 131: 105001

Fan J R, Du R, Gao S Y, Cao S B, Li X C, Peng Y Z (2024a). High-rate nitrite production by stable denitrification granular sludge in a reinforced-mixing up-flow system: shift in spatiotemporal characteristics of functional bacteria and metagenomic mechanisms. ACS Sustainable Chemistry & Engineering, 12(45): 16781–16790

Fan J R, Du R, Li C, Liu Q T, Peng Y Z (2022). Inducing high nitrite accumulation via modulating nitrate reduction power and carbon flux with *Thauera* spp. selection. Bioresource Technology, 354: 127188

Fan J R, Du R, Liu Q T, Li C, Peng Y Z (2024b). Microbial response and spatial profiling of nitrite-producing denitrification granular sludge *in-situ* exposed to high nitrite stress. Chemical Engineering Journal, 481: 148404

Feng J, Zhao J, Xiang H, You Z P, Shi L L, Yu Z D, Qiu Y L, Yu D S, Wang X X (2025). Establishment of continuous flow partial denitrification biofilm module with short hydraulic retention time. Water Research, 268: 122743

Franco A, Roca E, Lema J M (2006). Granulation in high-load denitrifying upflow sludge bed (USB) pulsed reactors. Water Research, 40(5): 871–880

Guo Y, Xie C L, Chen Y J, Urasaki K, Qin Y, Kubota K, Li Y Y (2021). Achieving superior nitrogen removal performance in low-strength ammonium wastewater treatment by cultivating concentrated, highly dispersive, and easily settleable granule sludge in a one-stage partial nitritation/anammox-HAP reactor. Water Research, 200: 117217

He J G, Xu J, Yu H R (2021). Performance and bacterial community dynamics of aerobic granular sludge working at low temperature enhanced by melamine framework embedding. Journal of Environmental Chemical Engineering, 9(2): 105156

Hou Y P, Peng D C, Wang B B, Zhang X Y, Xue X D (2014). Effects of stirring strategies on the sludge granulation in anaerobic CSTR reactor. Desalination and Water Treatment, 52(34−36): 6348–6355

Huang H, Ma R, Ren H Q (2024). Scientific and technological innovations of wastewater treatment in China. Frontiers of Environmental Science & Engineering, 18(6): 72

Kiehl J, Ben-Azzouz C, Dentel D, Derivaz M, Bischoff J L, Delaite C, Bistac S (2013). Grafting process of ethyltrimethoxysilane and polyphosphoric acid on calcium carbonate surface. Applied Surface Science, 264: 864–871

Kumari S, Tishel R, Eisenbach M, Wolfe A J (1995). Cloning, characterization, and functional expression of *acs*, the gene which encodes acetyl coenzyme A synthetase in *Escherichia coli*. Journal of Bacteriology, 177(10): 2878–2886

Li Y L, Zhang W J, Dai Y, Su X M, Xiao Y Y, Wu D, Sun F Q, Mei R W, Chen J R, Lin H J (2022). Effective partial denitrification of biological effluent of landfill leachate for Anammox process: start-up, influencing factors and stable operation. Science of the Total Environment, 807: 150975

Liu J G, Zhou Z Y, Li P Y, Wang Z X, Yan Y, Yu X Z, Li W K, Zheng T L, Cao Y N, Wu W J, et al. (2024). Characteristics of rural domestic sewage discharge and their driving mechanisms: evidence from the Northern Region, China. Frontiers of Environmental Science & Engineering, 18(7): 83

Liu S L, Zhou M, Daigger G T, Huang J P, Song G F (2023). Granule formation mechanism, key influencing factors, and resource recycling in aerobic granular sludge (AGS) wastewater treatment: a review. Journal of Environmental Management, 338: 117771

Ma J, Liu H, Dang H Z, Wu X B, Yan Y, Zeng T X, Li W W, Chen Y Z (2023). Realization of nitrite accumulation in an autotrophic-heterotrophic denitrification system using different S/N/C ratios coupled with ANAMMOX to achieve nitrogen removal. Journal of Chemical Technology and Biotechnology, 98(1): 269–281

Majjane A, Chahine A, Et-Tabirou M, Echchahed B, Do T O, Breen P M (2014). X-ray photoelectron spectroscopy (XPS) and FTIR studies of vanadium barium phosphate glasses. Materials Chemistry and Physics, 143(2): 779–787

Pinho F T, Piqueiro F M, Proençla M F, Santos A M (1997). Power and mean flow characteristics in mixing vessels agitated by hyperboloid stirrers. The Canadian Journal of Chemical Engineering, 75(5): 832–842

Qin C B, Xue Q, Zhang J W, Lu L, Xiong S G, Xiao Y, Zhang X J, Wang J N (2024). A beautiful China initiative towards the harmony between humanity and the nature. Frontiers of Environmental Science & Engineering, 18(6): 71

Qu J H, Chen J P (2024). Pathways toward a pollution-free planet and challenges. Frontiers of Environmental Science & Engineering, 18(6): 67

Soriano-Baguet L, Grusdat M, Kurniawan H, Benzarti M, Binsfeld C, Ewen A, Longworth J, Bonetti L, Guerra L, Franchina D G, et al. (2023). Pyruvate dehydrogenase fuels a critical citrate pool that is essential for Th17 cell effector functions. Cell Reports, 42(3): 112153

Sun C Y, Mao S Y, Zhao W Y, Chen Y S, Cao X, Tian T, Ma X Y, Li B, Qiu Y (2025). Multi-objective comparison of conventional and emerging wastewater treatment processes based on simulation to reduce greenhouse gas emissions. Frontiers of Environmental Science & Engineering, 19(3): 29

Tang C J, Zheng P, Wang C H, Mahmood Q, Zhang J Q, Chen X G, Zhang L, Chen J W (2011). Performance of high-loaded ANAMMOX UASB reactors containing granular sludge. Water Research, 45(1): 135–144

Wang B, Wu D, Zhang X L, Mackey H R, Chen G H (2018). Sludge flotation, its causes and control in granular sludge upflow reactors. Applied Microbiology and Biotechnology, 102(15): 6383–6392

Wang W Q, Li D, Li S, Li Z, Mu T W, Zeng H P, Zhang J (2022). Effect mechanism of shear stress on hollow anammox granules in low strength wastewater treatment. Journal of Environmental Chemical Engineering, 10(3): 107696

Xu D Y, Cao S B, Berry M, Du R, Peng Y Z (2023). Granulation of partial denitrification sludge: advances in mechanism understanding, technologies development and perspectives. Science of the Total Environment, 904: 166760

Zhang J W, Peng Y Z, Li X C, Du R (2022). Feasibility of partial-denitrification/ anammox for pharmaceutical wastewater treatment in a hybrid biofilm reactor. Water Research, 208: 117856

Zhang X Y, Wang B B, Han Q Q, Zhao H M, Peng D C (2013). Effects of shear force on formation and properties of anoxic granular sludge in SBR. Frontiers of Environmental Science & Engineering, 7(6): 896–905

Zhang Y, Zhang Z Z, Chen Y G (2021). Biochar mitigates N_2O emission of microbial denitrification through modulating carbon metabolism and allocation of reducing power. Environmental Science & Technology, 55(12): 8068–8078